PAPER

Check for updates

High-performance planar Zn-ion micro-capacitors†

Yujia Fan,[a] Xiaopeng Liu,[a] Nibagani Naresh,[a] Yijia Zhu,[a] Iman Pinnock,[a] Tianlei Wang,[b] Mingqing Wang, [ID][a] Ivan P. Parkin [ID][b] and Buddha Deka Boruah [ID] *[a]

Planar Zn-ion-based micro-capacitors (ZIMCs) present intriguing potential due to their unique blend of characteristics: battery-like anode properties and supercapacitor-like cathode attributes, offering intermediate energy storage capabilities with higher energy density than supercapacitors, superior power density compared to batteries, long-term cycling stability, slow self-discharge rates, and compatibility with ambient air processing. While electrodeposition facilitates the loading of Zn onto microelectrodes, incorporating high-capacity activated carbon cathode materials onto microelectrodes poses challenges, especially when the interdigitated electrode gap is less than 300 μm. Nevertheless, narrowing this gap is crucial to enhance ion transport, reduce charge transfer resistance, and maximize the effective utilization of the device's active area within its footprint. This study aims to achieve efficient loading of Zn and activated carbon onto gold interdigitated micro-electrodes to develop high-performance ZIMCs, utilizing a straightforward Microplotter technique capable of loading diverse materials onto microelectrodes effectively. The formed ZIMCs exhibit superior charge storage performance, including an areal energy of 1.2 μW h cm^{-2} at an areal power of 46.56 μW cm^{-2}, and 77% capacity retention after 1000 cycles. Further, our ZIMCs shows slow self-discharge response with only 26% voltage drop after 30 h.

Introduction

In an age of shrinking sizes and a growing need for compact, efficient energy storage solutions, the concept of planar microscale energy storage systems has emerged as a promising and inventive path.[1,2] As our world transitions to a more interconnected and IoT-driven landscape, the demand for energy storage technologies that can seamlessly fit into various applications has become increasingly evident.[3,4] Traditional energy storage methods have long been dominated by batteries and supercapacitors, each tailored to specific needs with their own unique features. However, the recent surge in demand for safer and high-performing devices has prompted the exploration of fresh energy storage systems. Planar Zn-ion micro-capacitors (ZIMCs) possess the potential to meet these modern demands by leveraging their inherent advantages. The distinctive characteristic of ZIMCs is their unique combination of a battery-type anode and an electrical double-layer capacitor-type cathode.[5,6] This configuration provides charge storage properties that deliver energy density surpassing that of supercapacitors, while simultaneously offering a power density exceeding that of traditional batteries.[7,8] Moreover, ZIMCs offer abundance and environmental friendliness. Their flat architecture simplifies their design, making them suitable for efficient spatial utilization and seamless integration into microelectronics, sensors, and other emerging technologies. Electrodeposition, a convenient technique, allows for selective material deposition on planar interdigitated electrodes (IDEs). For instance, electrodeposition of Zn onto metal IDEs for planar devices is straightforward.[5] However, the primary challenge lies in loading cathode materials with high electrical double-layer properties, such as activated carbon (AC). Commonly used techniques, such as screen printing,[9] 3D printing,[10] and mask-assisted spray processing,[11] facilitate cathode material loading. Nonetheless, these methods encounter difficulties with microelectrode gaps narrower than 300 μm. Therefore, it becomes imperative to efficiently load high-capacity cathode materials (e.g., AC) and subsequently narrow the IDE gap. This approach enhances ion transport, reduces charge transfer resistance, and maximizes the utilization of the active device area within its footprint.

Consequently, an advanced technique is needed to load various high-capacity materials, especially AC, onto ZIMC IDEs. This report delves into the utilization of an advanced Microplotter technique for effectively loading AC and Zn anode materials selectively onto Au IDEs with a 200 μm electrode gap.

[a]Institute for Materials Discovery, University College London, London WC1E 7JE, UK. E-mail: b.boruah@ucl.ac.uk

[b]Department of Chemistry, University College London, London, WC1H 0AJ, UK

† Electronic supplementary information (ESI) available. See DOI: https://doi.org/10.1039/d4ta00300d

This technique facilitates efficient and selective material loading onto the desired device area without material-loading limitations. Furthermore, the ZIMCs exhibit charge storage capabilities, with an impressive areal energy of 1.2 μW h cm^{-2}, remarkable capacity retention of 77% even after 1000 cycles, and a slow self-discharge rate, maintaining 74% voltage retention even after 30 hours. Consequently, these techniques hold the potential to introduce novel approaches for integrating high-capacity materials onto microelectrodes, enabling the development of high-performance micro-scale energy storage devices.

Results and discussion

Efficiently loading high-capacity active materials onto microelectrodes is essential as it significantly influences the overall performance of microscale energy storage systems. In the intricate process of creating ZIMCs, Au IDEs having a spacing of 200 μm between these electrodes on insulating substrates were used, as visually depicted in Fig. 1a(i). This initial step sets the foundation for the subsequent stages. Following this, the dynamic procedure involves the loading of two distinct materials – Zn and AC – onto respective Au IDEs. This crucial task is
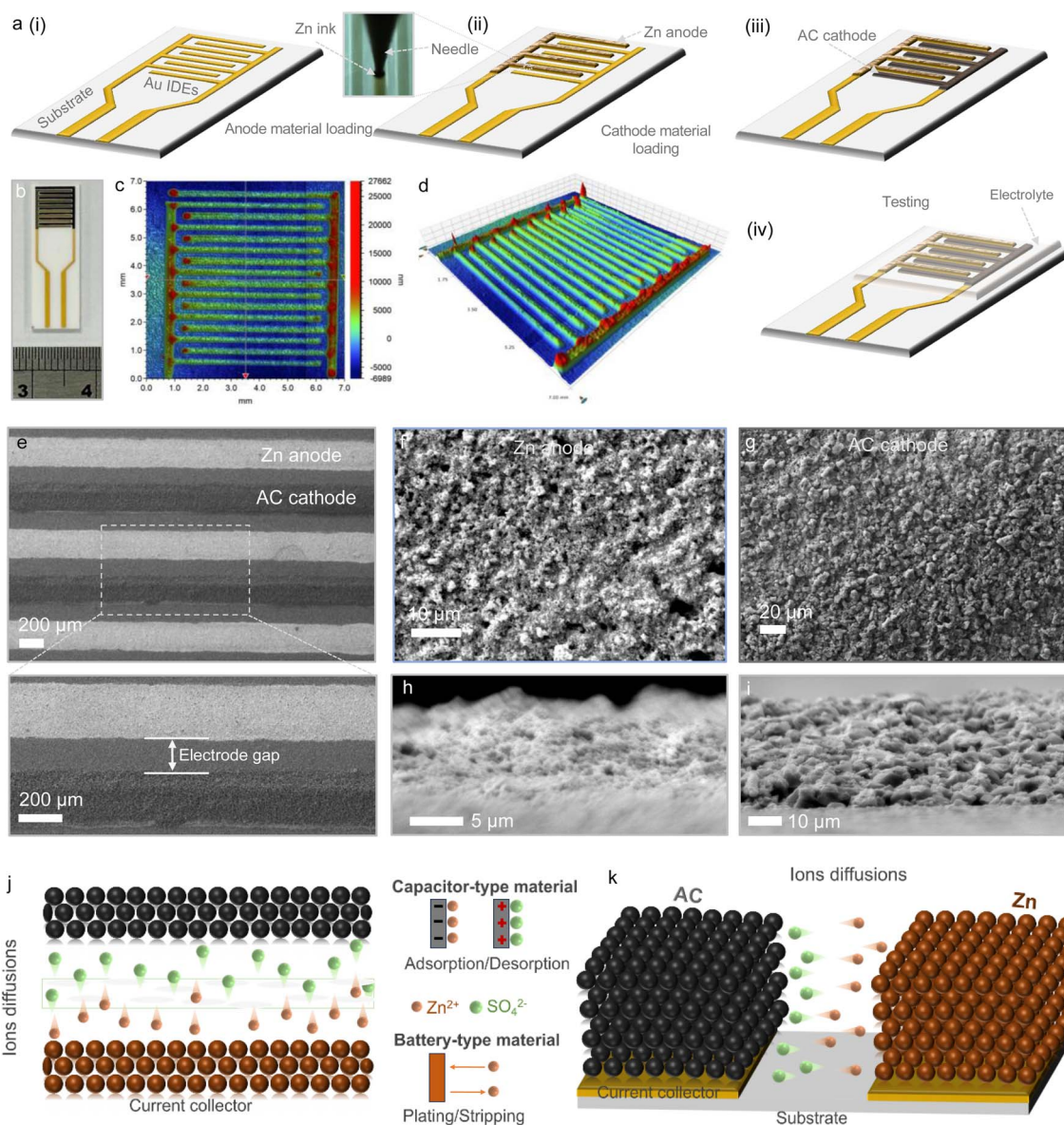

Fig. 1 (a) Illustration depicting the sequential stages involved in the creation of ZIMCs. (i) Patterning of Au IDEs with a 200 μm gap on insulating substrates. (ii and iii) Loading of active materials: Zn on the anode and AC on the cathode current collectors, accomplished using the Microplotter technique. (iv) Testing of the fabricated ZIMCs. (b) A digital image of a ZIMC. (c and d) 2D and 3D profilometer mappings of the developed ZIMC. (e) SEM images of a ZIMC. (f and g) Magnified SEM images of the Zn anode and AC cathode materials loaded onto Au IEDs. (h and i) Cross-sectional SEM images revealing the microelectrodes' Zn and AC compositions. (j and k) Schematic illustration depicting the diffusion of ions in both conventional sandwich-type and planar-type ZIMCs, followed by the adsorption/desorption of ions on the capacitor-type AC cathode and the plating/stripping of ions on the battery-type Zn anode during the charging and discharging processes.

artfully accomplished by harnessing the capabilities of the Microplotter technique, as showcased in Fig. 1a(ii) and (iii). In the inset of Fig. 1a(ii), the micropipette nozzle boasts an inner diameter of 20 μm, a capability surpassing that of alternative printing methods in achieving high resolution. The micropipette is affixed to a piezoelectric ceramic, which, in turn, connects to the controller *via* wires. These wires facilitate the application of voltage, inducing vibrations in the micropipette. By controlling the voltage magnitude, precise modulation of ink deposition onto the substrate is achieved. The delicate balance in ink optimization, elaborated in the Experimental section, holds the key to obtaining the desired outcome. Through diligent optimization and a series of deliberate testing and printing sequences, the processing of these ZIMCs was precisely refined. The resultant ZIMCs, embodying the essence of precision engineering, underwent rigorous testing within a gel electrolyte milieu, where Fig. 1b shows the digital image of a ZIMC. Moving beyond the surface, Fig. 1c and d capture the ZIMC's essence in both 2D and 3D representations (profilometer images). The average surface thickness of the device measures approximately 16 μm, with the initial thickness of the Au IDE being about 6 μm. Consequently, the thickness of the printed electrode layer is approximately 10 μm. This imagery serves to underscore the achievement of successful active material loading onto the planar Au IDEs, devoid of any impediments such as short-circuits or ink leakage. Fig. 1e reveals the scanning electron microscope (SEM) image of a ZIMC at different magnifications, and Fig. 1f and g show magnified top-view SEM images, enabling the observation of the Zn anode and AC cathode materials of the ZIMC. These images distinctly highlight the uniformity and consistent distribution of active materials across the Au IDEs, a testament to the precision achieved through the fabrication process. Delving deeper, the investigation extends to cross-sectional images in Fig. 1h and i, where the anode's Zn and cathode's AC composition are brought into focus, respectively. This introspective exploration confirms, once again, the even-handed and systematic loading of active materials onto the Au IDEs. The ion diffusion mechanism in planar-type ZIMCs differs from that in conventional sandwich-type ZIMCs. Specifically, planar-type ZIMCs exhibit in-plane ion diffusion, as illustrated in Fig. 1j and k.

Progressing further, our inquiry takes a closer look at the inherent qualities of the Zn and AC materials in use. This is achieved through thorough materials characterization, a crucial step to unlock the potential of these components. The detailed insights gained from SEM and TEM imaging, as demonstrated in Fig. 2a–e, offer a glimpse into the morphologies of these materials. In Fig. 2a and b, the Zn nanoparticles exhibit particle sizes that span from 40 nm to 150 nm. The high-resolution TEM, displaying a measured d-spacing of ~0.134 nm corresponding to the (103) plane of hexagonal zinc, is corroborated in Fig. 2c. On the other hand, the AC particles present a more diverse range of sizes (Fig. 2d and e), indicating the inherent variation in their composition. In the realm of material crystallography, the XRD patterns (Fig. 2f and g) provide valuable insights into the atomic arrangement within the Zn nanoparticles and AC powders. Fig. 2f shows the XRD of Zn

nanoparticles, where the characteristic peaks observed at around $2\theta = 36.1°$, $38.8°$, $43.1°$, and $54.2°$ and $69.9°$ correspond to the (002), (100), (101), (102) and (103) planes of hexagonal zinc, refereeing to PDF#87-0713. Moreover, in Fig. 2g, the characteristic peaks of AC positioned at around $2\theta = 22°$ and $43.7°$ correspond to the reflections of the (002) and (101) facets, respectively, where the broadening of characteristic peaks denotes that AC is in an amorphous state. Transitioning to Fig. 2h, we delve into the Raman spectrum of the AC material. The Raman spectrum displays distinctive features, including a D band centered at approximately 1341.7 cm^{-1}, which corresponds to regions characterized by disorder and structural defects, primarily composed of sp^3 hybridized carbon atoms. Additionally, there is a G band at around 1591.6 cm^{-1}, which corresponds to the stretching of the C=C bond found in graphitic carbon regions characterized by sp^2 hybridized carbon systems.[12] The calculated intensity ratio of these peaks (I_D/I_G) stands at 0.97 (<1), which means that the carbon exhibits partial crystallinity alongside structural disorder in the arrangement of its atoms, corresponding to amorphous structure of AC. Furthermore, two additional peaks at higher wavenumbers are observed, specifically around 2688.8 cm^{-1} (2D) and 2910.3 cm^{-1} (S3), which are attributed to the overtone of carbon and indicate the presence of a few-layered carbon material.[13] This observation further supports the graphitic nature of the AC material. One of the most noteworthy attributes of AC is its specific surface area, a characteristic that holds immense significance in energy storage applications. The calculation of 1585.53 m^2 g^{-1} (as demonstrated in Fig. 2i, through a BET isotherm plot) emphasizes the extensive surface area that AC offers. This high surface area is particularly desirable for promoting electrical double-layer capacitance, a phenomenon that can greatly enhance the energy storage capacity of the system. This observation forms the bedrock for the subsequent discussions on achieving high-performance ZIMBs (as elaborated further). X-ray photoelectron spectroscopy (XPS) findings were elaborated from Fig. S1.† In Fig. S1a,† the Zn 2p peak displayed discernible split spin–orbit components (Zn 2p$_{1/2}$ and Zn 2p$_{3/2}$). Analysis of the O 1s spectra of Zn (Fig. S1b†) revealed two distinct peaks upon curve fitting: one at 530.7 eV and another at 532.8 eV, corresponding to oxygen–metal bonds and adsorbed oxygen. This indicates slight oxidation of Zn nanoparticles due to exposure to ambient air. Regarding the XPS examination of AC in Fig. S1c and S1d,† no evidence of a C–C bond was observed in the C 1s spectra. Peaks observed in the O 1s spectra at 531.6 eV, 533 eV, and 534.8 eV indicated O–C=O, C=O, and C–O bonds, respectively.

Subsequently, we evaluated the charge storage performance of the prepared ZIMC in a gel electrolyte, which involved dissolving ZnSO$_4$ into a gelatin matrix to form the gel. Detailed information on the preparation of the gel electrolyte can be found in the Experimental section (ESI†). After assembling the prepared gel electrolyte (please refer to the digital image of the electrolyte, Fig. S2a†), we assessed the electrochemical performance of the ZIMCs. This was accomplished by immersing the device directly into a cuvette filled with the electrolyte (Fig. S2b†) and allowing it to solidify for a few hours before testing.
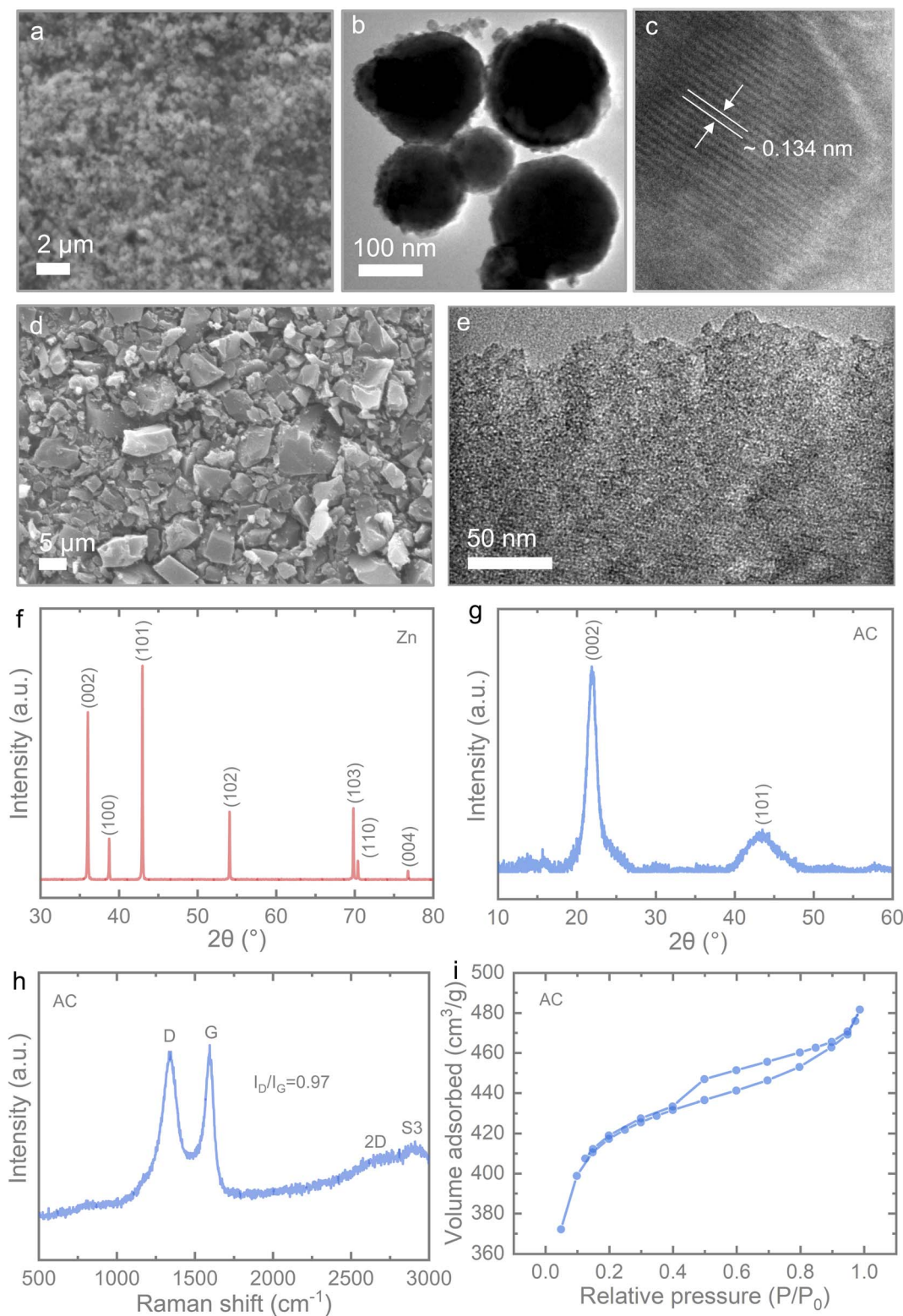
Fig. 2 (a and b) SEM and TEM images of Zn nanoparticles, verifying sizes ranging from 40 nm to 150 nm. (c) High-Resolution TEM confirming a measured d-spacing of ~0.134 nm corresponding to the (103) planes of hexagonal Zn. (d and e) SEM and TEM images illustrating the morphology of the employed AC powders. (f and g) XRD patterns depicting the structural characteristics of hexagonal Zn nanoparticles and amorphous AC. (h) Raman spectrum of AC revealing discernible peaks associated with the D and G bands, with a peak intensity ratio of 0.97 ($=I_D/I_G$). (i) Assessment of AC's specific surface area through a BET isotherm plot, yielding a calculated specific area of 1585.53 $m^2 g^{-1}$.

Initially, we conducted Cyclic Voltammetry (CV) of the ZIMC at various scan rates, ranging from 10 mV s^{-1} to 500 mV s^{-1}, within the voltage range of 0.6 V to 1.4 V. During the charging process, Zn^{2+} cations plating onto the Zn anode take place to offer battery-type charge storage, while anions adsorbtion onto the AC for electrical double-layer capacitance-based charge
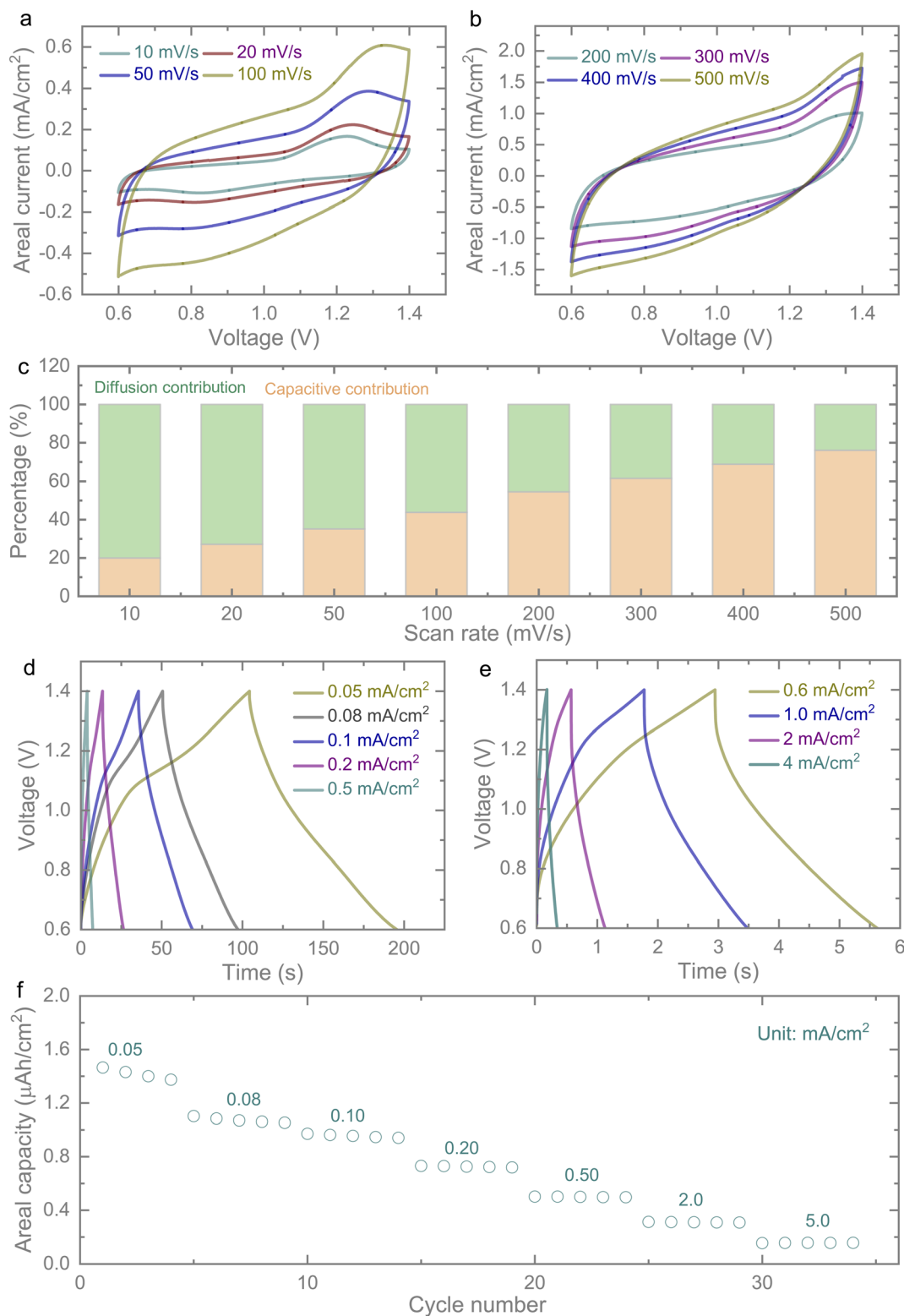

Fig. 3 CV characteristics of the ZIMC at varying scan rates, specifically (a) in the range of 10 to 100 mV s^{-1} and (b) spanning from 200 to 500 mV s^{-1}. (c) Capacitive and diffusion contribution plot with respect to the scan rate. (d) and (e) GCD profiles at different areal currents, namely 0.05 to 0.5 mA cm^{-2} and 0.6 to 4.0 mA cm^{-2}, within the voltage range of 0.6 to 1.4 V. (f) The rate test results for the ZIMC.

storage. During discharging, Zn^{2+} ions strip from the Zn anode, and desorption of ions from the AC cathode take place (Fig. 1h and i).[14,15] In Fig. 3a, the CV curves obtained at relatively low scan rates of 10, 20, 50, and 100 mV s^{-1} exhibit an identical CV pattern, indicating a stable charge storage response for our ZIMC. However, slight distortion in the CV curves was observed when testing our ZIMC at relatively high scan rates of 200 to 500 mV s^{-1} (Fig. 3b), potentially attributable to the limited ionic conductivity of the gel electrolytes, leading to polarization effects. The process of charge storage can be analysed in terms of capacitive-controlled ($k_1 v$) and diffusion-controlled ($k_2 v^{0.5}$) components, as indicated by the current at a fixed voltage relationship, $I(V) = k_1 v + k_2 v^{0.5}$ or $I(V)/v^{0.5} = k_1 v^{0.5} + k_2$. Utilizing this equation, the overall capacitive contribution can be calculated to be approximately 35% and 76% at scan rates of 50 mV s^{-1} and 500 mV s^{-1} (Fig. 3c and S3†). To gain a more comprehensive understanding of the charge storage performance of the ZIMC, we conducted galvanostatic charge–discharge (GCD) tests at various areal current densities, ranging from 0.05 to 5.0 mA cm^{-2}, within the voltage window of 0.6 to 1.4 V. As illustrated in Fig. 3d, the GCD profiles at relatively low areal currents of 0.05 to 0.5 mA cm^{-2} consistently maintained a uniform pattern, reaffirming the stable charge storage response across different areal currents. Based on these GCD profiles, the calculated areal capacities were 1.44 µA h cm^{-2}, 0.95 µA h cm^{-2}, and 0.5 µA h cm^{-2} at areal currents of 0.05 mA cm^{-2}, 0.10 mA cm^{-2}, and 0.50 mA cm^{-2}, respectively. Furthermore, even at higher areal currents (Fig. 3e), the measured areal capacities were 0.31 µA h cm^{-2} (at 2.0 mA cm^{-2}) and 0.16 µA h cm^{-2} (at 5.0 mA cm^{-2}), affirming the high-performance characteristics of the ZIMC. Additionally, the rate test plot (Fig. 3f) confirmed the consistent maintenance of stable areal capacities across various areal currents. When increasing the areal currents from 0.05 to 5.0 mA cm^{-2}, the ZIMC continued to exhibit a capacity retention of 11.11%, underscoring its high-rate capability within micro-scale energy storage systems.

Moreover, the self-discharge phenomenon in micro-scale energy storage devices, particularly micro-supercapacitors, has been a significant concern, primarily attributed to the ohmic leakage, which arises from the resistive pathway between the positive and negative electrodes. Parasitic faradaic reactions, such as the oxidation or reduction of species on the electrode surface, potentially lead to energy loss. Charge redistribution, stemming from unequal charge distribution during the charging process, can cause the movement of the charge barrier over time.[16] Therefore, the suppression of self-discharge in micro-scale energy storage devices is of utmost importance, and effective strategies are required. These strategies may include electrode surface modifications, electrolyte adjustments, the inclusion of ion-exchange membranes (for conventional energy storage systems), and the efficient loading of energy materials onto microelectrodes. This last aspect is particularly crucial for micro-scale devices. To comprehend the self-discharge behaviour of our ZIMC, we conducted a study by charging the ZIMC to its maximum voltage of 1.4 V and subsequently measuring self-discharge over time, as depicted in Fig. 4a. Interestingly, we observed only a 26% voltage reduction, indicating 74%

retention, even after 30 hours of self-discharging. This level of voltage retention surpasses that of previously reported micro-supercapacitors. For instance, in Fe–MnO$_2$ symmetric micro-supercapacitors, a 50% voltage reduction occurred within 12 hours;[17] meanwhile in 3D printed graphene-based symmetric micro-supercapacitors, a 50% voltage reduction took place within 3 hours;[18] AC-based symmetric micro-supercapacitors experienced a 50% voltage reduction within 2.5 hours;[19] laser-written rGO-based symmetric micro-supercapacitors saw a 50% voltage drop within less than 1 hour;[20] in MnO$_2$-PPy//V$_2$O$_5$-PANI asymmetric micro-supercapacitors, a 53% voltage reduction occurred within 1.1 hours;[21] laser-written GO film-based symmetric micro-supercapacitors showed a 50% voltage drop within 13 hours;[22] hexacyanoferrate/graphene hybrid thin film-based asymmetric micro-supercapacitors witnessed a 48% voltage reduction within 3 hours,[23] respectively. This suggests that our observed ZIMC demonstrates an exceptionally slow self-discharge rate, sustaining a consistent voltage reading of 1.04 V for an extended duration. This phenomenon could be attributed to the collective charge storage mechanisms, including battery-like behavior on the Zn anode and electrical double-layer characteristics on the AC electrodes. Additionally, the open circuit voltage of the ZIMC exceeds 1.1 V, contrasting with the typical millivolt range of common supercapacitors, which further contributes to the slow self-discharge behavior.

Furthermore, we conducted extended cycling stability tests on our ZIMC, as depicted in Fig. 4b. These tests revealed a capacity retention of 77% after 1000 cycles when tested at 0.1 mA cm^{-2}. The relatively low capacity fading of 23% after 1000 cycles serves as a confirmation of the charge storage stability offered by our ZIMC. To gain a deeper understanding of electrode stability, we investigated the SEM cycling, as depicted in the insets of Fig. 4b and S4.† It was observed that the morphologies of the Zn NPs anode underwent a transformation into vertically oriented 2D sheet-like structures, attributed to the preferred growth direction of Zn.[24] Conversely, no significant morphological changes were noted in the AC. To further assess the stability of the electrode materials, postmortem XRD and Raman analyses were conducted on cycled electrode materials over 1000 cycles in a coin cell configuration, as conducting XRD and Raman tests on a printed ZIMC posed challenges. The comparison of XRD patterns (refer to Fig. S5a†) revealed a slight leftward shift in the peaks of Zn without altering the crystal structure.[24] Additionally, the Raman spectra of AC (Fig. S5b†) exhibited a slight increase in the intensity ratio of D and G bands after cycling, indicating heightened edge defects due to the adsorption and desorption of zinc ions. These findings align with the operational mechanism of zinc ion hybrid capacitors.[25] Meanwhile, our ZIMCs exhibited a low equivalent series resistance of 11.4 ohms, as shown in Fig. 4c. In addition to this, our ZIMCs showcased outstanding charge storage performance with areal energies of 1.2 µW h cm^{-2} at 46.56 µW cm^{-2} and 0.26 µW h cm^{-2} at 1841 µW cm^{-2} (volumetric energy of 120 µW h cm^{-3} at a volumetric power of 4.656 mW cm^{-3} and 26 µW h cm^{-3} at 184.1 mW cm^{-3}). These values surpass the performance of most previously reported high-performance symmetric and asymmetric micro-
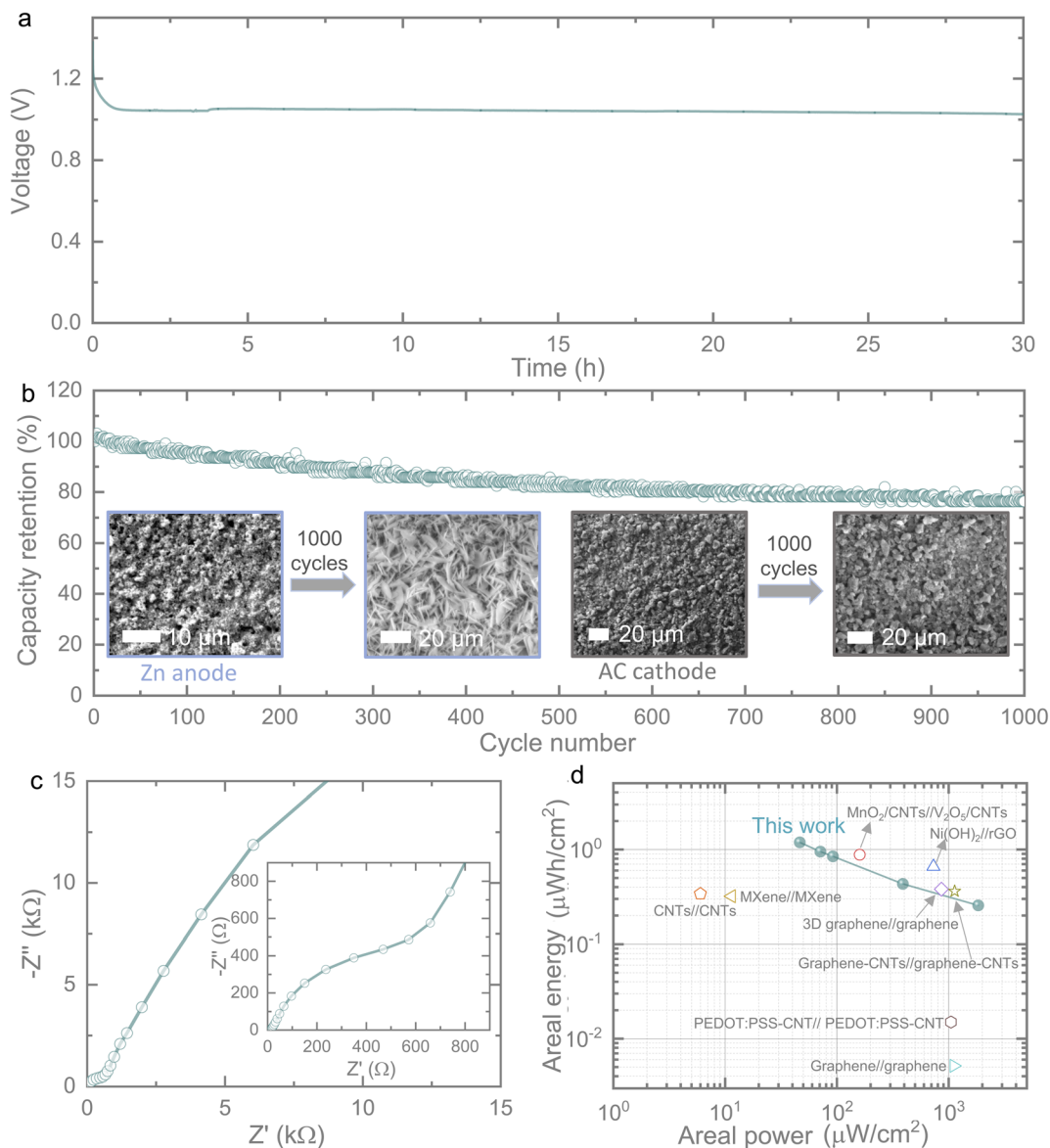
Fig. 4 (a) Self-discharge assessments of the ZIMC, illustrating a mere 26% voltage decrease during self-discharging over 30 hours. (b) Extended cycling trials at 0.1 mA cm^{-2} for 1000 GCD cycles, revealing an impressive 77% capacity retention. Insets show the SEM images of the Zn anode and AC cathode before and after 1000 cycles. (c) Nyquist plot of the ZIMC confirming a low equivalent series resistance of 11.4 ohms. (d) Ragone plot providing a comparative representation of our ZIMC with previously reported micro-supercapacitors, encompassing both symmetric and asymmetric designs.

supercapacitors (Fig. 4d). For instance, our ZIMCs outperformed micro-supercapacitors such as graphene//graphene with 0.0056 µW h cm^{-2} at 1112 µW cm^{-2},[26] PEDOT:PSS-CNT// PEDOT:PSS-CNT with 0.015 µW h cm^{-2} at 1050 µW cm^{-2},[27] CNTs//CNTs with 0.34 µW h cm^{-2} at 6 µW cm^{-2},[28] MXene// MXene with 0.32 µW h cm^{-2} at 11.4 µW cm^{-2},[29] MnO$_2$-CNTs// V$_2$O$_5$-CNTs with 0.88 µW h cm^{-2} at 160 µW cm^{-2},[30] Ni(OH)$_2$// rGO with 0.66 µW h cm^{-2} at 730 µW cm^{-2},[31] 3D graphene// graphene with 0.38 µW h cm^{-2} at 860 µW cm^{-2},[32] and graphene-CNTs//graphene-CNTs with 0.36 µW h cm^{-2} at 1130 µW cm^{-2},[33] respectively. Furthermore, we employed a combination of two ZIMCs to illustrate the variations in voltage and charge when integrated in series and parallel configurations

(Fig. S6a,† as depicted schematically). As illustrated in Fig. S6b and S6c,† the series integration of two ZIMCs extended the voltage range from 0.6–1.4 V to 0.6–2.2 V, evident in both the CV and GCD profiles, while parallel integration resulted in an increased current in the CV and a longer discharge time in the GCD. Therefore, depending on the specific requirements, the voltage and current from the ZIMCs can be adjusted through their integration. For example, the seamless integration of two ZIMCs in series is well-suited to power a moisture sensor (an indoor and outdoor thermometer with a hygrometer clock) as shown in Fig. S6d.†

In conclusion, this study is centered on the development of high-performance planar ZIMCs through the effective loading

of active materials onto micro-electrodes using the Microplotter technique. The ZIMCs presented here, which combine a high-capacity battery-type Zn anode with a supercapacitor-based AC cathode, exhibit remarkable charge storage performance. This includes enhanced areal energy and areal power, measured at 1.2 μW h cm^{-2} and 46.56 μW cm^{-2}, as well as cycling stability, with 77% capacity retention after 1000 cycles. Moreover, the ZIMC system demonstrates a notably slow self-discharge rate, with only a 26% voltage loss even after 30 hours, which is significantly lower than that observed in planar micro-supercapacitors. As a proof-of-concept experiment, the Micro-plotter technique holds great promise for effectively loading high-energy materials onto microelectrodes in high-performance planar micro-scale energy storage devices.

Experimental section

Materials

The zinc nanoparticles, which had an average size ranging from 40 to 150 nm, was sourced from Sigma Aldrich. The activated carbon was obtained from MTI Corporation, and the triethylene glycol monomethyl ether (TEGMME) was supplied by Sigma Aldrich. It's important to note that all these chemicals were utilized without the need for additional purification.

Preparation of zinc and activated carbon inks

In a vessel, 4 g of triethylene glycol monomethyl ether (TEGMME) and 6 g of zinc nanopowder were combined, and a tip sonicator (Fisherbrand 505 Sonicator) was employed for a 30 minute sonication process. The sonicator was set to an amplitude of 30% with a pulse configuration of 01 01. For the preparation of the activated carbon ink, 4 g of TEGMME and 2.5 g of activated carbon underwent a 30 minute sonication process using the same sonicator settings.

Printing of ZIMCs

The zinc and activated carbon inks were applied *via* a SonoPlot Microplotter Proto, equipped with a 20 μm nozzle, onto gold interdigitated electrodes (IDEs) featuring a 200 μm gap between the electrodes (obtained from Metrohm U.K. Ltd., model DRP-IDEAU200-U50). Prior to the printing process, the ZIMC pattern was designed using SonoDraw software. To enhance the adhesion between the inks and the substrates, the IDEs underwent a pre-cleaning process involving acetone, followed by exposure to UV ozone treatment for a duration of 5 minutes, utilizing an Ossila UV Ozone Cleaner. During the printing operation, the starting point of the pattern was aligned with the nozzle, and the feature width was configured to 50 μm. The printing voltage applied was 8 V for the zinc ink and 12 V for the activated carbon ink, utilizing the spraying mode.

Material characterization

To examine the morphology and microstructure of the raw materials, namely zinc and activated carbon powder, we utilized scanning electron microscopy, specifically a ZEISS Sigma 500 Field Emission Scanning Electron Microscope. In addition, we employed Raman spectroscopy, utilizing a RENISHAW inVia Raman microscope, to gain insights into the crystalline information of these powders. Furthermore, we assessed the crystalline properties of the powders by means of X-ray diffraction, performed using a Malvern Panalytical Aeris X-ray diffractometer. To explore the specific surface area of the activated carbon, we conducted BET measurements using the NOVAtouch instrument. To create a 3D mapping of the printed ZIMCs, we employed a stylus profilometer, specifically a DektakXT from Bruker. XPS analysis was conducted using a Thermo NEXSA G2 XPS instrument equipped with a monochromated Al kα X-ray source (energy of 1486.7 eV), a spherical sector analyzer, and three multichannel resistive plate detectors with 128 channels each. All measurements were carried out at a power of 19.2 W with an X-ray beam size of 400 × 200 μm. Survey scans were performed with a pass energy of 200 eV, while high-resolution scans were conducted with a pass energy of 50 eV. Electronic charge neutralization was accomplished using an ion source (Thermo Scientific FG-03) with an ion gun current of 150 μA and an ion gun voltage of 40 V. Sample data acquisition was executed under a pressure below 10^{-8} Torr at room temperature (294 K). Data analysis was performed using CasaXPS v2.3.26rev1.0N, with peaks fitted against a Shirley background prior to component analysis.

Electrochemical testing

The fabrication process of the printed ZIMCs involved immersing them in a gel electrolyte, which was prepared by dissolving 2 g of gelatin in 15 mL of 1 M zinc sulfate (ZnSO$_4$) electrolyte. To assemble the device, two pieces of copper foil were affixed to the electrode ends using silver paste, and the junctions were subsequently covered with Kapton tape. Next, the ZIMC was positioned within a cuvette (Fisherbrand Disposable Cuvettes 14955125), and the gel electrolyte was introduced into the cuvette.

The electrochemical evaluation of the ZIMCs encompassed various tests performed on battery testing systems (MPG2, BioLogic; Neware and IVIUM testers). These tests were conducted within a voltage range spanning from 0.6 to 1.4 V and included cyclic voltammetry (CV) at different scan rates ranging from 10 to 500 mV s^{-1}, galvanostatic charge–discharge (GCD) tests at various areal currents ranging from 0.05 to 5.0 mA cm^{-2}, long-term cycling at 0.1 mA cm^{-2} for 1000 cycles, and measurements of self-discharge. Additionally, electrochemical impedance spectroscopy (EIS) tests were carried out within a frequency range spanning from 10 mHz to 100 kHz at a voltage amplitude of 10 mV. These tests were conducted using an IVIUM Potentiostat/Galvanostat tester.

Conflicts of interest

The authors declare no competing financial interest.

References

1 J. H. Pikul and H. Ning, *Joule*, 2018, **2**, 1036–1038.
2 P. Li, M. Liao, J. Li, L. Ye, X. Cheng, B. Wang and H. Peng, *Small Struct.*, 2022, **3**, 2200058.

3 Q. Xia, F. Zan, Q. Zhang, W. Liu, Q. Li, Y. He, J. Hua, J. Liu, J. Xu, J. Wang, C. Wu and H. Xia, *Adv. Mater.*, 2023, **35**, 2200538.

4 S. Kim, A. Patra, R. R. Kohlmeyer, S. Jo, X. Yue, A. Johnson, C. T. Kiggins, B. Zahiri, K. Jeong, J. Koo, T. Kang, P. Sun, J. B. Cook, J. H. Pikul and P. V. Braun, *Cell Rep. Phys. Sci.*, 2023, **4**, 101205.

5 G. Sun, H. Yang, G. Zhang, J. Gao, X. Jin, Y. Zhao, L. Jiang and L. Qu, *Energy Environ. Sci.*, 2018, **11**, 3367–3374.

6 P. Zhang, Y. Li, G. Wang, F. Wang, S. Yang, F. Zhu, X. Zhuang, O. G. Schmidt and X. Feng, *Adv. Mater.*, 2019, **31**, 1806005.

7 Z. Cao, G. Liang, D. Ho, C. Zhi and H. Hu, *Adv. Funct. Mater.*, 2023, **33**, 2303060.

8 J. Yin, W. Zhang, N. A. Alhebshi, N. Salah and H. N. Alshareef, *Adv. Energy Mater.*, 2021, **11**, 2100201.

9 J. Zeng, L. Dong, L. Sun, W. Wang, Y. Zhou, L. Wei and X. Guo, *Nanomicro Lett.*, 2021, **13**, 19.

10 Z. Fan, J. Jin, C. Li, J. Cai, C. Wei, Y. Shao, G. Zou and J. Sun, *ACS Nano*, 2021, **15**, 3098–3107.

11 B. D. Boruah, *Energy Storage Mater.*, 2019, **21**, 219–239.

12 V. S. Bhat, P. Kanagavalli, G. Sriram, R. P. B, N. S. John, M. Veerapandian, M. Kurkuri and G. Hegde, *J. Energy Storage*, 2020, **32**, 101829.

13 G. K. Gupta, P. Sagar, S. K. Pandey, M. Srivastava, A. K. Singh, J. Singh, A. Srivastava, S. K. Srivastava and A. Srivastava, *Nanoscale Res. Lett.*, 2021, **16**, 85.

14 H. Wang, M. Wang and Y. Tang, *Energy Storage Mater.*, 2018, **13**, 1–7.

15 H. Tang, J. Yao and Y. Zhu, *Adv. Energy Mater.*, 2021, **11**, 2003994.

16 W. Shang, W. Yu, X. Xiao, Y. Ma, Y. He, Z. Zhao and P. Tan, *Adv. Powder Mater.*, 2023, **2**, 100075.

17 Y. Wang, Y.-Z. Zhang, Y.-Q. Gao, G. Sheng and J. E. ten Elshof, *Nano Energy*, 2020, **68**, 104306.

18 W. Li, Y. Li, M. Su, B. An, J. Liu, D. Su, L. Li, F. Li and Y. Song, *J. Mater. Chem. A*, 2017, **5**, 16281–16288.

19 C. Gao, J. Huang, Y. Xiao, G. Zhang, C. Dai, Z. Li, Y. Zhao, L. Jiang and L. Qu, *Nat. Commun.*, 2021, **12**, 2647.

20 W. Gao, N. Singh, L. Song, Z. Liu, A. L. M. Reddy, L. Ci, R. Vajtai, Q. Zhang, B. Wei and P. M. Ajayan, *Nat. Nanotechnol.*, 2011, **6**, 496–500.

21 Y. Yue, Z. Yang, N. Liu, W. Liu, H. Zhang, Y. Ma, C. Yang, J. Su, L. Li, F. Long, Z. Zou and Y. Gao, *ACS Nano*, 2016, **10**, 11249–11257.

22 M. F. El-Kady and R. B. Kaner, *Nat. Commun.*, 2013, **4**, 1475.

23 Y. He, P. Zhang, M. Wang, F. Wang, D. Tan, Y. Li, X. Zhuang, F. Zhang and X. Feng, *Mater. Horiz.*, 2019, **6**, 1041–1049.

24 A. D. Prasetya, M. Rifai and H. Miyamoto, *J. Phys. Conf. Ser.*, 2020, **1436**, 012113.

25 Y. Liu and L. Wu, *Nano Energy*, 2023, **109**, 108290.

26 L. Li, E. B. Secor, K. Chen, J. Zhu, X. Liu, T. Z. Gao, J. T. Seo, Y. Zhao and M. C. Hersam, *Adv. Energy Mater.*, 2016, **6**, 1600909.

27 W. Liu, C. Lu, H. Li, R. Y. Tay, L. Sun, X. Wang, W. L. Chow, X. Wang, B. K. Tay, Z. Chen, J. Yan, K. Feng, G. Lui, R. Tjandra, L. Rasenthiram, G. Chiu and A. Yu, *J. Mater. Chem. A*, 2016, **4**, 3754–3764.

28 H. Kim, J. Yoon, G. Lee, S. Paik, G. Choi, D. Kim, B.-M. Kim, G. Zi and J. S. Ha, *ACS Appl. Mater. Interfaces*, 2016, **8**, 16016–16025.

29 C. Zhang, L. McKeon, M. P. Kremer, S.-H. Park, O. Ronan, A. Seral-Ascaso, S. Barwich, C. Ó. Coileáin, N. McEvoy, H. C. Nerl, B. Anasori, J. N. Coleman, Y. Gogotsi and V. Nicolosi, *Nat. Commun.*, 2019, **10**, 1795.

30 J. Yun, Y. Lim, H. Lee, G. Lee, H. Park, S. Y. Hong, S. W. Jin, Y. H. Lee, S. Lee and J. S. Ha, *Adv. Funct. Mater.*, 2017, **27**, 1700135.

31 G.-W. Huang, N. Li, Y. Du, Q.-P. Feng, H.-M. Xiao, X.-H. Wu and S.-Y. Fu, *ACS Appl. Mater. Interfaces*, 2018, **10**, 723–732.

32 L. Zhang, D. DeArmond, N. T. Alvarez, R. Malik, N. Oslin, C. McConnell, P. K. Adusei, Y. Hsieh and V. Shanov, *Small*, 2017, **13**, 1603114.

33 S. Bellani, E. Petroni, A. E. Del Rio Castillo, N. Curreli, B. Martín-García, R. Oropesa-Nuñez, M. Prato and F. Bonaccorso, *Adv. Funct. Mater.*, 2019, **29**, 1807659.